Particuology 106 (2025) 291–304

Contents lists available at ScienceDirect

Particuology

journal homepage: www.elsevier.com/locate/partic

Marine inspired design of soil rippers using ship bulbous bow geometries: A cross-disciplinary approach with DEM simulation insights

Egidijus Katinas [a,*], Regita Bendikienė [a], Antanas Čiuplys [a], Rostislav Chotěborský [b], Monika Hromasová [b], Barbora Kuřetová [b]

[a] Kaunas University of Technology, K. Donelaičio St. 73, Lt-44249, Kaunas, Lithuania
[b] Czech University of Life Sciences Prague, Kamýcká 129, 165 00, Praha, Suchdol, Czech Republic

ARTICLE INFO

Article history:
Received 27 March 2025
Received in revised form
2 September 2025
Accepted 10 September 2025
Available online 20 September 2025

Keywords:
Soil ripper
Bulbous bow
Draught force
Discrete element method (DEM)
Agricultural machinery

ABSTRACT

Over the past decades, scientists have studied tillage and soil processing technologies based on the classical shapes of agricultural tools. Numerous studies highlight the importance of agricultural tool longevity in relation to abrasive wear resistance and draught force values. However, these studies are typically limited to the most common shapes and types of tools. This paper combines the insights gained from the marine industry's experience in the design of ship's bulbous bows with the challenges of designing soil rippers for agricultural machinery. New shape elements were developed based on the delta, oval, and nabla types of bulbous bows used in ships. Thirteen types of designed elements, along with the original shape, were tested virtually using the Discrete Element Method (DEM). The 3D-printed samples were then tested in a sand bin to measure draught force. DEM simulation parameters were validated by measuring the Static Angle of Repose (SAOR) of sand. The results of this study demonstrate that applying a bulbous bow-inspired shape to the soil ripper can reduce draught force by 7.1 %; however, in some cases, it can also increase the force by 4.1 % compared to the original shape. The values are giving statistically significant differences between the experimental measurements. To fully evaluate the application of these designed elements, further soil disturbance and wear analysis studies should be conducted in future research.

1. Introduction

Various techniques and engineering solutions have been adopted to improve soil processing (Liu et al., 2023; Sang et al., 2022), seedbed preparation (Gong et al., 2022; Zhang et al., 2024), reduce draught (tillage) force (Wang et al., 2023) and ensure soil loosening process (Barr et al., 2018) in agricultural works. The bio-inspired surfaces (Wang et al., 2019, 2020), coatings or tools (Guan et al., 2022; Sun et al., 2020) can suggest significant differences in soil processing changes and uses, especially the reduction of draught force. A bionic prototype taken from bear (Li et al., 2016), mole (Zhang et al., 2022) or a bodger claw (Xu et al., 2024) reduced the draught force from 7.8 to 22.4 % compared with subsoiler with an arc-shape shank (Wang et al., 2023). Even nanocoatings (such as titanium nitride and tantalum carbide) have a much lower coefficient of friction and adhesion compared to other surfaces (Mehrang Marani et al., 2019). By combining two different scientific fields, newly developed tools can be applied.

Most of the previously mentioned literature sources provide data based on modelling and laboratory/field experiments. Soil is a granular, highly specific material that requires extensive knowledge and experimental testing to validate results. The Discrete Element Method (DEM) completely fulfils soil properties and gives it to numerical applications. The numerical methods allow shortening the design phase during the prototyping, as failures can be seen during the virtual testing phase. For example, it can help to analyse soil-tool-crop residue interactions (Adajar et al., 2021; Zhao et al., 2024) or abrasive wear analysis can be performed by the DEM to estimate the longevity of soil processing tool (Ge et al., 2023; Ma et al., 2023; Schramm et al., 2020). Additionally, DEM-

* Corresponding author.
E-mail address: egidijus.katinas@ktu.lt (E. Katinas).

https://doi.org/10.1016/j.partic.2025.09.011

based semi-autogenous grinding mill (SAG mill) technology (Bao et al., 2025; Xie et al., 2022) helps analyse and address the smoothing of lifter edge shapes due to wear. Saving materials allows reducing greenhouse emissions and climate change, which are the main directions of the European Union and the World.

The European Union's Green Deal Common Agricultural Policy (CAP) takes demand on no-tillage technology (Guyomard et al., 2020). No-tillage technology of sugar beet growing can have the lowest energy and carbon emission cost (Šarauskis et al., 2018). This technology is based on agroecological principles, where soil rotation and disturbance are minimal. There were 98.1 million hectares of arable land used in the EU in 2020, but only 3.7 % of arable area was processed by zero tillage technology (Ec.europa.eu, 2024). The statistics show that the no-till has potential. However, this specific technology requires a specific shape of tooling, where the soil ripper tool opens the soil and prepares the seedbed. Furthermore, soil has a high abrasivity which causes large wear losses.

In most of cases, agricultural tools are wide (from 80 mm and more) and heavy (2 kg and more), specially reinforced with layer of hardfacing or tungsten carbide plates (Fig. 1). These reinforcements help to reduce abrasive wear and extend the tool's longevity (Kostencki et al., 2016) but they can also increase energy costs for soil processing.

During the tilling process the abrasive wear outcome for the ripper can be 60–120 g ha^{-1} (Bayhan, 2006; Natsis et al., 2008). As a result of this damage, farmers suffer high downtime during the season, and economic losses are caused by increased demand for material, which affects climate change.

The first test of the soil ripper with a pyramid-shape hard alloy tip (Jankauskas et al., 2014) with a sharp edge, a round shape is obtained after processing an area of 46 ha. The same soil ripper tip was used to estimate stress and motion work when finite element analysis helped to analyse it. For ease of evaluation, the cutting edge of 3D element (tip) was rounded by a certain radius (Skirkus et al., 2016), as the cutting edge of the real-shaped tip had a similar round shape.

According to the previous wear analysis (Katinas et al., 2019) related to the soil ripper, it was found that at the deepest working depth, the plate also transforms into the round shape. Sharp corners are rounded after 208 km of wear track in the soil (Fig. 2). The wear intensity depends on the alloy type and the shape of the ripper element (tool). An alternative to the polygonal surface is the bulbous bow shape element used in the marine industry (Liu et al., 2021; Tran et al., 2021).

Knowledge of the marine industry inspired to the design of bulbous bow for an agriculture tool. Bulb types can be classified according to three shapes (Hoyle, 1985; Kracht, 1978) (Fig. 3): delta (Δ) (the shape of the drop), oval (O) (mass centre in the middle), and nabla (∇) (an upside-down shape of the drop (delta)) type bulbs.

According to literature, blunt narrow openers with 90° rake angles can had higher force compared to sharper tools design. It can be explained that blunt geometry form wider soil wedges and less streamlined flow, which influences force prediction (Aikins et al., 2023) but otherwise the flat front surface can suffer higher pressure concentration at the point of impact forming dense shear bands. Tool geometry directly affects wear because it influences the conditions at the interface between the tool and the processed soil. Parameters such as edge radius, rake angle, and overall shape determine the distribution of forces, material flow, and the generation of frictional heat during machining. Sharp geometries typically concentrate stress at contact points, increasing the likelihood of abrasive wear, while blunt or rounded edges can distribute forces more evenly but increase the contact area, promoting adhesive wear. In addition, certain geometries can influence chip formation, surface interaction, all of which contribute to the dominant wear mechanisms. Therefore, even small changes in tool geometry can result in significant differences in wear rates and wear patterns.

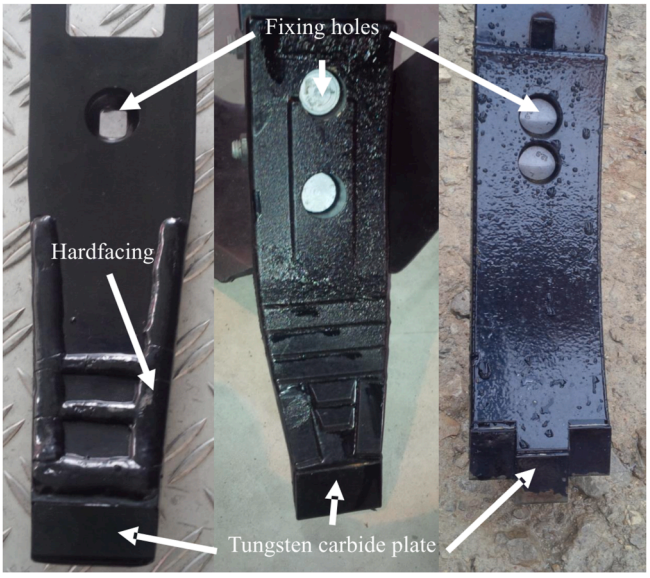

Fig. 1. Reinforced agricultural tools.

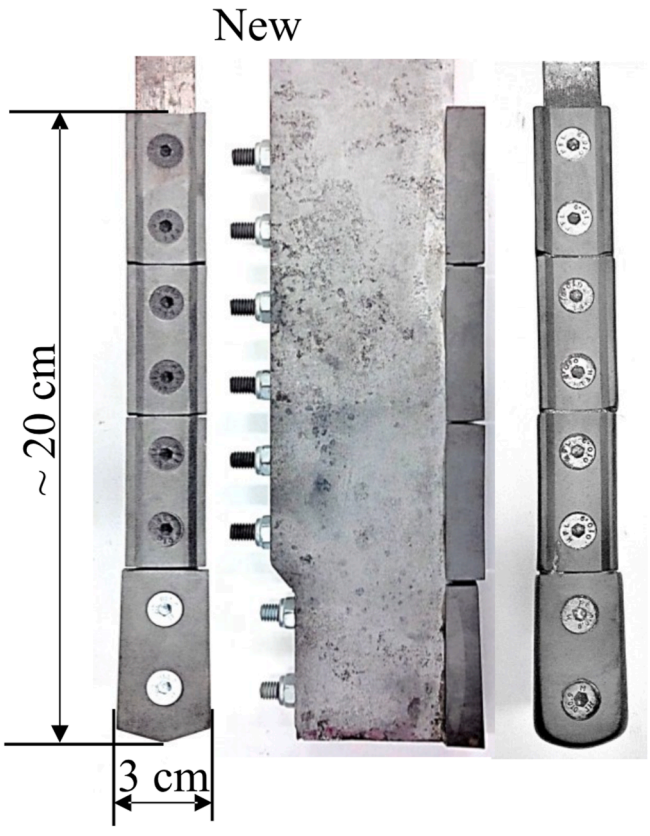

Fig. 2. Soil ripper with wear resistant hard facings: new and worn (208 km wear track) (Katinas et al., 2024).

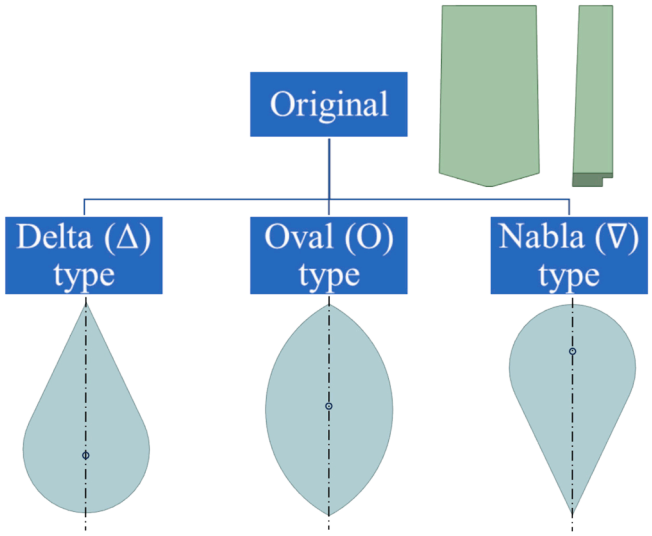

Fig. 3. Ship bulb types prepared according to Kracht (Kracht, 1978).

The field experiment of a newly designed bulbous bow shape element will take a long time and require a lot of finance, because the bulb shaped element may fail due to increased draught force or low soil disturbance. DEM is a tool that shortens the design process step to avoid the failure improper bulb shape and simultaneously measures the draught force to compare results with the original soil ripper tool element.

In the most of cases, literature introduces particle displacement and soil disturbance of vertically curved soil processing tools as subsoilers tines, ploughshares and mouldboards, cultivator tines, etc. (Bao et al., 2023; Kalácska et al., 2020; Yao et al., 2024; Zhang et al., 2022), but there is no particle flow analysis of sphere-shaped tools in agricultural applications. It leads to the space to investigate bulbous bow shaped element analysis in the agriculture.

This study aims to design, simulate, and experimentally validate the bulbous bow elements for a soil ripper tool in a sand bin. The obtained draught force values allow to compare the simulation results of the discrete element method with the laboratory test. By considering the force and energy reduction of the designed elements, the most valuable shape can be selected for future field experiments to study longevity in real time.

2. Materials and methods

2.1. Bulbous bow design

Elements for the soil ripper have been developed and modified based on the bulbous bow types mentioned above. These elements are designed according to the following criteria:

- The width of the element should not be too large compared to the original shape of the element (±35 mm);
- The height of the element should be similar to the original element (±54 mm).

The size of designed elements should be closer to the original due to soil processing and disturbance. However, the larger area (greater width or height) of a larger element increases the draught force of the tool and energy consumption (Gürsoy et al., 2017; Jiang et al., 2020). Previous field experiments (Katinas et al., 2019) have shown that a height of 54 mm for removable elements adequately meets maintenance expectations if the elements are lost or damaged because of contact with the stone. The higher width of the element is unnecessary because the main part (tine) where the hard alloy elements are mounted has a width of 20 mm. Likewise, the increasing of sweep tine width has linear increase of the draught force (Ucgul et al., 2014). The designed elements are shown in Fig. 4. These elements are divided into three groups to maintain the delta, oval and nabla shapes. The dimensions of the elements are given in Table 1. The designed delta (D1–D3) and nabla N1–N3 elements are similar in size and shape but nabla (N1–N3) elements have an inverted shape. The oval O1 and O2 are identically shaped elements with small edges on the top and bottom to protect the central part of the ripper. The O3 element has smaller dimensions than the original and other oval elements. The O4 element (oval type) is the widest (35 mm) compared to the oval type of group elements. Elements N4–N6 are slightly different in dimensions from previous nabla-type elements (N1–N3). These elements based on delta, oval and nabla shape would assist as an extra mass or volume reserve for the wear loss during the soil processing. It will improve the longevity and wear resistance.

The 3D printed samples had high surface irregularities. To evaluate surface roughness of 3D printed samples were used the laser scanner Prince 335 Handheld 3D. The scanning accuracy 0.020 mm + 0.08 mm m^{-1}.

2.2. DEM model

The DEM methodology employed is divided into two phases: Static Angle of Repose (SAOR) calibration and the virtual sand bin test. An angle of repose test method was used to calibrate the silica sand parameters for DEM tests. Subsequently, the sand bin test was performed to measure the draught force. The setup and parameters are explained in the following subsections.

2.2.1. SAOR calibration

SAOR is commonly used in engineering and material science to calibrate the parameters of granular material in numerical models (Nouh et al., 2024; Xu et al., 2023). SAOR represents the steepest slope of unconfined material, measured from the horizontal plane, on which the material can be stacked without collapsing (Makange, Ji, & Torotwa, 2020; Xie et al., 2022).

Silica sand was used as the granular material in this study. A cylindrical tube (inner diameter: 100 mm) was placed on a horizontal surface, filled with sand, and then raised at a constant speed (0.00325 m s^{-1}), allowing the granular material to form a conical shape (Fig. 5). The SAOR was measured along the side of the conical pile. To obtain accurate material parameters for simulation, the test was carried out in the laboratory and the results were compared with simulations created using Ansys Rocky software (Ansys, 2024). A software script helped evaluate the simulated results. The methodology of SAOR simulation and laboratory measurement followed the approach described in the literature (Černilová et al., 2024; Černilová et al., 2022), where the SAOR of rapeseed and sand were measured.

Fig. 6(a) presents the simulation results, where the script shows the average (black dots) maximum particle height, the dashed regression lines (black and red) indicate the estimated SAOR, the light red area represents the maximum height of the particles, and the dark red region shows the lowest height of the particles in the conical pile (Ansys, 2024). The SAOR measurement of the laboratory study is shown in Fig. 6(b). GeoGebra online software (geogebra.org) was used to process the pile images taken during the laboratory SAOR measurement.

The SAOR simulation DEM parameters are described in Table 2. The SAOR test is mainly influenced by the friction coefficients of

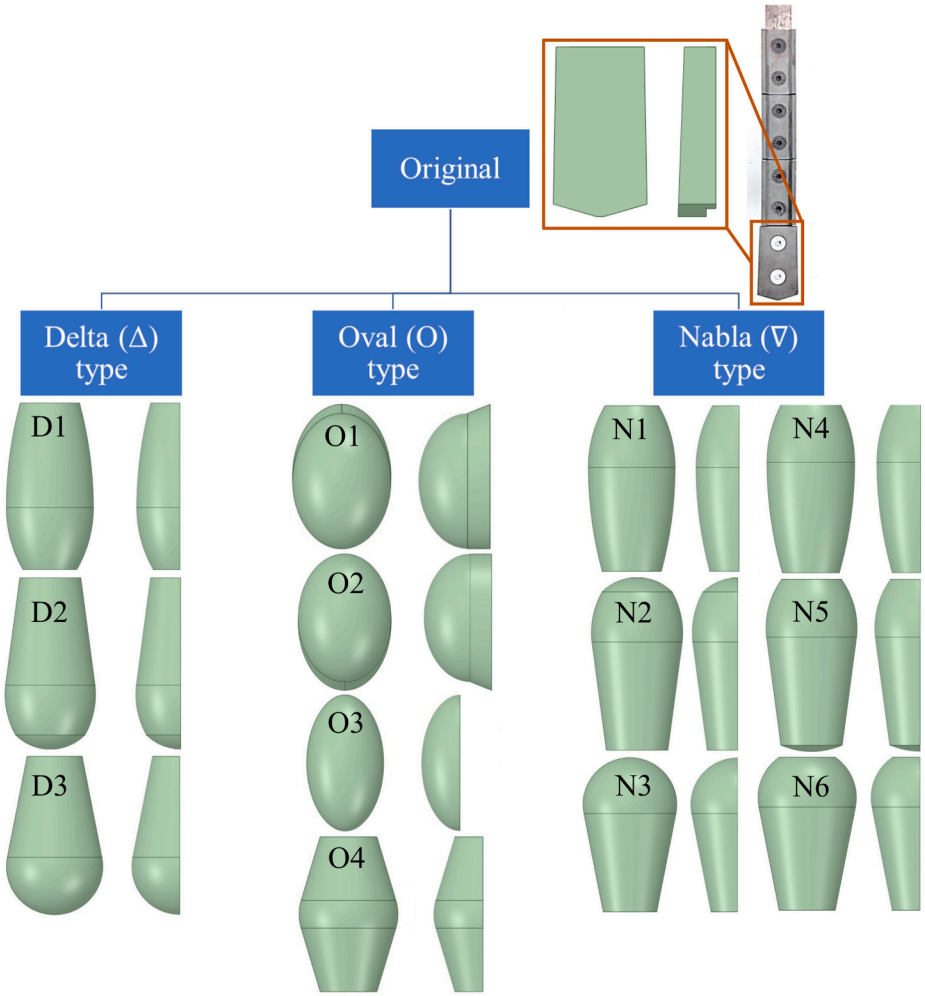

Fig. 4. Delta, oval and nabla shaped types of elements designed for the soil ripper.

Table 1
Maximum width, height and depth of designed elements (in mm).

Designed element		Width	Height	Depth	Element
Original		30	54	12	
Delta	D1	29	56	15	
	D2	30	56	15	
	D3	35	58	18	
Oval	O1	32	47	23	
	O2	32	47	23	
	O3	26	46	13	
	O4	35	54	17	
Nabla	N1	29	56	15	
	N2	30	56	15	
	N3	35	58	18	
	N4	29	56	18	
	N5	30	56	15	
	N6	35	54	18	

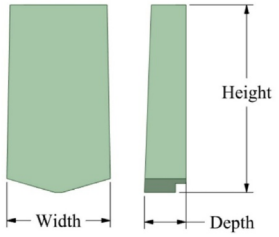

sand-sand and rolling friction (Roessler & Katterfeld, 2016). According to researchers (Just et al., 2013; Nouh et al., 2024), the angle of repose is more influenced by static friction than by rolling resistance. The laboratory SAOR study showed a SAOR of 29.73 ± 0.18° (Fig. 6(b)), while the DEM simulation gave results of 29.6 ± 0.08° (Fig. 6(a)). These results were obtained when the coefficients of static and dynamic friction were 0.7 and 0.6, respectively, and the coefficient of rolling resistance was 0.14 (Table 2). These calibrated coefficients were used for further simulations in the virtual sand bin experiment.

2.2.2. Virtual sand bin test

The size of virtual sand bin is 0.5 × 1.5 × 0.25 m, filled with a spherical particle with a diameter of 0.005 m (Fig. 7). The working depth of tool was 0.1 m, and working speed was 0.1 m s^{-1}. The simulation time was 11 s (travel distance 1.1 m), with a time step of

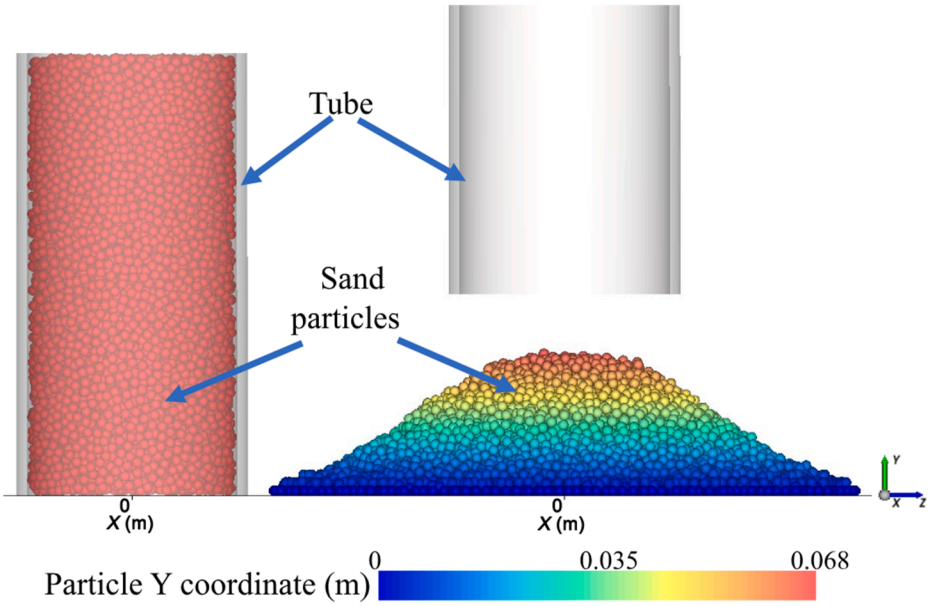

Fig. 5. Simulation of the static angle of repose (SAOR) test.

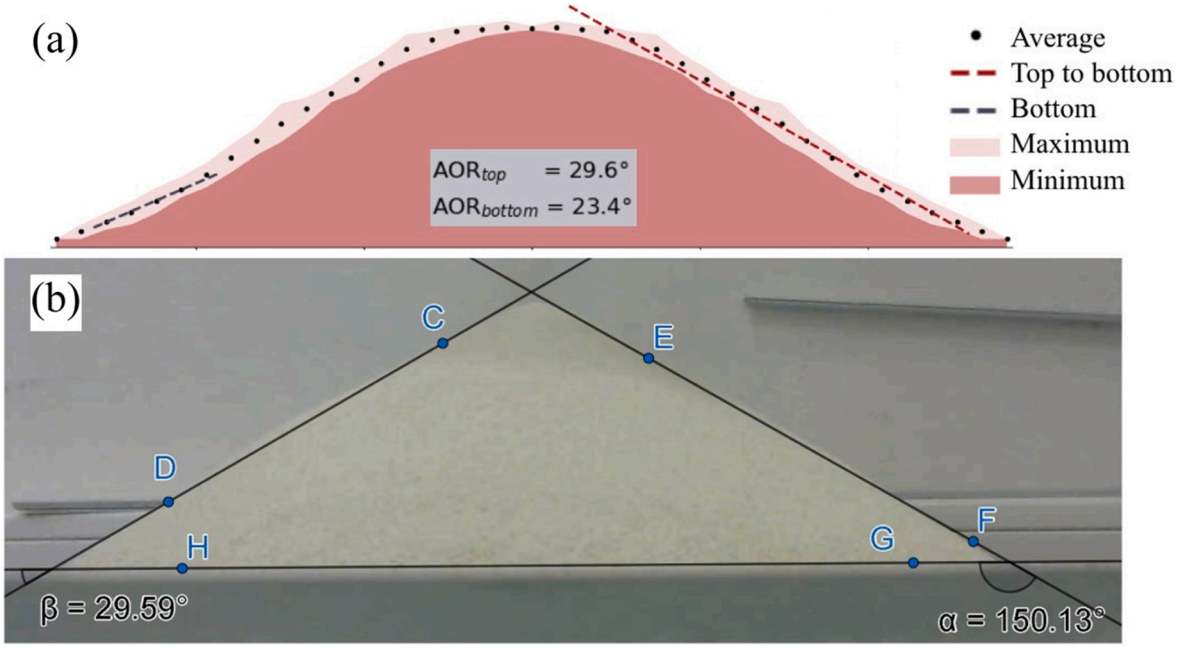

Fig. 6. Static angle of repose verification: (a) simulation, (b) laboratory test.

0.01 s for saving data. The sample (bulbous bow element) mesh was created by the ANSYS Workbench platform using nonlinear mechanical physics preference with a mesh of 3 mm and a holder (shank) of10 mm. DEM simulation parameters and interaction properties based on the study of Kuře et al. (2021) described in Table 2. The normal force was described as a hysteretic linear spring, and the tangential force was Coulomb limit models of the linear spring.

The hysteretic linear spring model presented by Walton and Braun (1986) is an elastic-plastic (repulsive and dissipative) normal contact model. This enables the simulation of plastic energy dissipation during contact, avoiding the computational cost associated with longer simulation times. Furthermore, since there is no viscous damping term in the model, the energy dissipation remains independent of the relative velocities between neighbouring particles, ensuring that it is not affected by other contacts. Another notable benefit of this model is its ability to accurately represent compressible materials, as contact forces can approach zero value even in presence of residual overlaps. The following equations represent the hysteretic linear spring model implemented in Ansys Rocky software (Ansys, 2024):

$$F_n^t = \begin{cases} \min\left(F_n^{t-\Delta t} + K_{nu}\Delta S_n, K_{nl}S_n^t\right) \text{ if} \Delta S_n \geq 0 \\ \max\left(F_n^{t-\Delta t} + K_{nu}\Delta S_n, 0,001K_{nl}S_n^t\right) \text{ if} \Delta S_n < 0 \end{cases} \quad (1)$$

Table 2
DEM parameters of sand particles, geometry and their interaction (Kuře et al., 2021).

Parameters		Value
Sand properties		
Gravity (m s^{-2})		9.81
Bulk density (kg m^{-3})		1533
Particle size (m)		0.005
Poisson's ratio		0.3
Young Modulus (MPa)		1.7
Rolling resistance		0.14
Geometry properties		
Density (kg m^{-3})		1020
Poisson's ratio		0.3
Young modulus (MPa)		2200
Material interaction properties	Sand-sand	Sand-geometry
Static friction	0.7	0.4
Dynamic friction	0.6	0.3
Tangential stiffness ratio	1	1
Restitution coefficient	0.3	0.3

$$\Delta S_n = S_n^t - S_n^{t-\Delta t} \tag{2}$$

where F_n^t and $F_n^{t-\Delta t}$ are normal elastic-plastic contact forces at the current time t and at previous time $t - \Delta t$, respectively, where Δt is the time step, ΔS_n is the change in the contact normal overlap at the current time (Fig. 8). It is considered positive when the particles are moving toward each other and negative when they are moving apart. S_n^t and $S_n^{t-\Delta t}$ are the normal overlap values at current and at previous time respectively. K_{nl} and K_{nu} are the stiffness values of the loading and unloading contact, respectively.

The tangential force in this model is elastic-frictional (linear spring-coulomb limit models). If the tangential force were considered to be fully elastic, its value at time t calculated from the equation (Ansys, 2024):

$$F_{t,e}^t = F_t^{t-\Delta t} + K_t \Delta S_t \tag{3}$$

where $F_t^{t-\Delta t}$ is the value of the tangential force at a previous time, ΔS_t is the tangential relative displacement of the particles during the timestep, K_t is the tangential stiffness. The elastic-plastic normal contact model is appropriate for simulating non-adhesive and dry granular materials (sand).

Particle rolling resistance is applied to rearrange the particle shape effects for spherical particles. The DEM simulation used a C-type rolling resistance model: a linear spring rolling limit to compensate the effect of surface irregularities (non-sphericity)

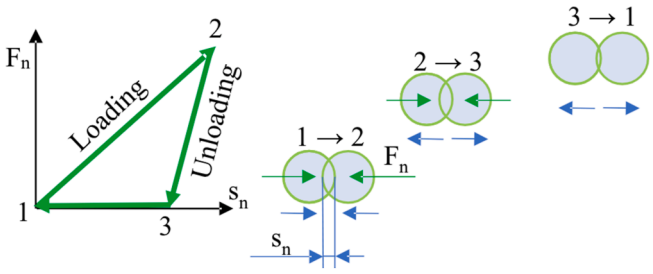

Fig. 8. Normal force overlap according to the hysteretic linear spring model (Walton & Braun, 1986).

and particle shape (Wensrich & Katterfeld, 2012). According to Wensrich and Katterfeld (2012), a suitable rolling stiffness value ensures good rolling resistance behavior without the need of additional damping. This approach is followed in Rocky (Ansys, 2024), where the rolling stiffness (K_r) is defined as:

$$K_r = R_r^2 K_\tau \tag{4}$$

where K_τ is the t tangential stiffness (multiplying the ratio of normal stiffness to tangential stiffness defined by user), R_r is the rolling radius, calculated as follows:

$$\frac{1}{R_r} = \begin{cases} \frac{1}{|r_1|} + \frac{1}{|r_2|} & \text{particle} - \text{particle} \\ \frac{1}{|r|} & \text{particle} - \text{geometry} \end{cases} \tag{5}$$

where r_1 and r_2 are the rolling radius of the particles in contact, r is the rolling radius of the particles in contact with the geometry. The rolling radius vector is defined as the vector connecting the centroid of the particle and the point of contact at a given time.

$$M_{r,e}^t = M_r^{t-\Delta t} - K_r \omega_{rel} \Delta t \tag{6}$$

where $M_r^{t-\Delta t}$ is the vector of the moment of rolling resistance (Fig. 9) in the previous time step, ω_{rel} is the vector of the relative angular velocity, which is defined as the difference between the angular velocities of the two particles in contact or the angular velocity of a particle on a boundary, Δt is the simulation timestep. The updated moment of rolling resistance is not directly used in the particle motion equation. In the C-type rolling resistance model, the magnitude of the rolling resistance moment is limited

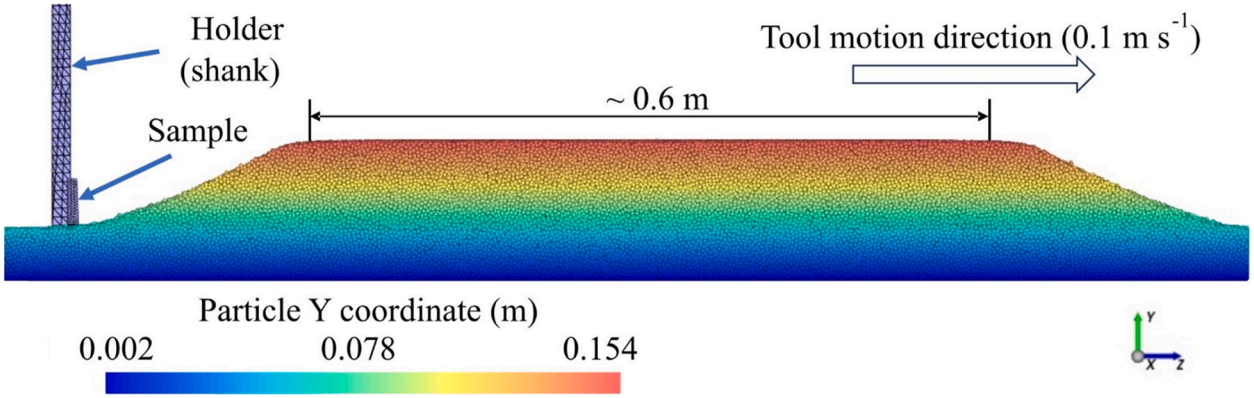

Fig. 7. Virtual sand bin filled with sphere particles (Katinas et al., 2024).

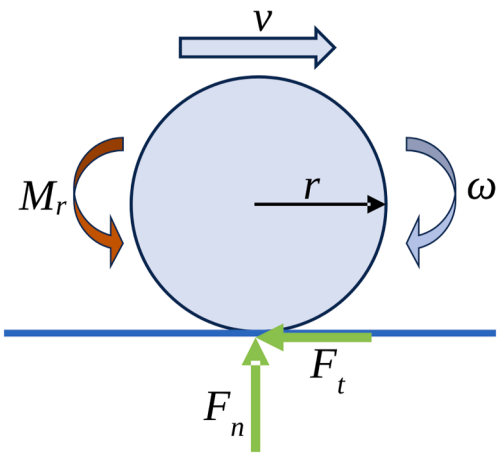

Fig. 9. Particle affected by rolling resistance moment.

by the value achieved at full mobilization rolling angle. The limit value is:

$$M_{r,lim} = \mu_r R_r F_n \tag{7}$$

where μ_r is the rolling resistance coefficient, Rocky defines as a particle property simply listed as rolling resistance. This dimensionless parameter represents the tangent of the maximum slope angle at which the moment of rolling resistance counterbalances the moment produced by gravity acting on the particle. R_r is the rolling radius and F_n is the normal force at the contact. According to Eqs. (6) and (7), the C-type rolling resistance moment model (linear spring rolling limit) can be described as:

$$M_\tau^t = \min\left(\left|M_{r,e}^t\right|, M_{r,lim}\right)\frac{M_{r,e}^t}{\left|M_{r,e}^t\right|} \tag{8}$$

2.3. Sand bin test

A laboratory sand bin (Fig. 10) test is used to compare the DEM simulation with the actual measurement. The design of the equipment allows to measure the draught force of the designed elements. The measurement method is used as described in the work of Kuře et al. (2021). The printed elements (delta, oval and nabla) are attached to the holder, and the working depth in the sand is set to 0.1 m. The holder is an aluminium square tube (20 × 20 × 2 mm). The sand bin is filled with silica sand of fraction 0.1–0.3 mm (density: 2650 kg m^3, moisture content: 0 %). The tool

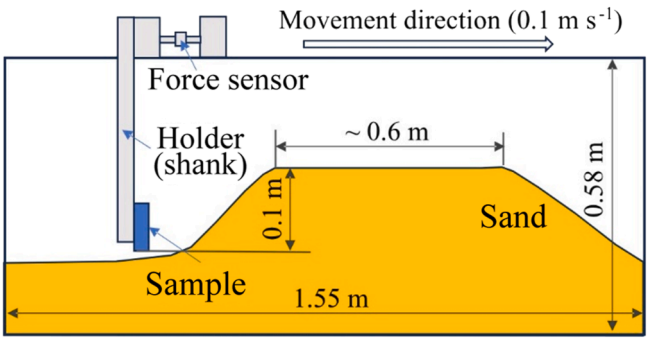

Fig. 10. Draught force measurement in a sand bin.

motion speed is 0.1 m s^{-1}. A force sensor attached to the holder and frame shows a draught force value during sand processing. The force sensor's (LCMFD-2KN) maximum measured force is 2 kN (accuracy ≤500 N: ±0.15 %). The experiment was repeated three times with each type of element.

3. Results and discussion

This section presents the draught force results as influenced by the design area, discusses the effects of 3D printing layers, and suggests ideas future work on wear analysis of bulbous bow elements.

3.1. Draught force and consumed energy results

This section describes the draught force results for all types of designed elements inspired by the bulbous bow. There are fourteen results for the draught force of the designed elements. Due to the large number of results, the most representative are presented here: the draught force results for the original (Org), delta (D1), oval (O1) and nabla (N1) shaped elements are shown in Figs. 11 and 12. The trend of the draught force is similar to the simulation and experimental measurements. The force increases after contact with sand particles and reaches its highest value in the middle of the bin (around 0.4 m). In the second part of the travel distance, it begins to decrease, as the resistance of the holder with the sample passes through the pile of sand (particle).

One of the most critical factors in evaluating the serviceability of newly designed elements is the maximum value of draught force. Estimating the maximum draught force is difficult because it fluctuates during sand processing. The average draught force in the middle sand bin was calculated to obtain the best results. According to the curves in Figs. 11 and 12, the steady state of the maximum draught force is in the range of 0.3–0.5 m sand processing distance. This section calculates the average draught force for each element. However, the area limited by the draught force and travel distance values allows the energy required to process the sand to be calculated through simulation and experimentation. An example of energy calculation is presented in Fig. 13. The green-coloured area is the energy required to drag the original (Org) shape sample with a holder at the travel distance of 0.3–0.5 m. The calculated draught force and energy results of designed elements are given in Table 3.

Tracking of the particle's trajectory during the simulated sand processing helps to see interaction between the sample surface and particles itself. In Fig. 14, it is possible to track particle motion of Org and O3 samples. Near the flat front surface of Org sample (Fig. 14(b)) can be seen nicely arranged particle layer which works as protective shield and particles trajectory has longer horizontal trajectory lines (Fig. 14(a)), compared to O3 sample (Fig. 14(c)) where the trajectory lines are shorter. The particles are not creating an arranged layer on the sphere surface of sample O3 (Fig. 14(d)) and their motion more directed to the sides of the sample because it is creating protrusion effect as a ship with bulbous bow in a water.

Based on the draught force data (Table 3), the simulation showed higher values than the experimental measurement in the range of 0.9–12.2 %. However, considering the values of the standard error (which shows how close the sample mean is to the population mean (Curran-everett, 2008)), most simulation and experiment results are not significantly different. The statistical evaluation by ANOVA showed that there is a statistically significant difference between the simulation and experiment measured draught force because the p-value is less than the significance level (0.05). Except the O1 and O3 has p-values higher than the

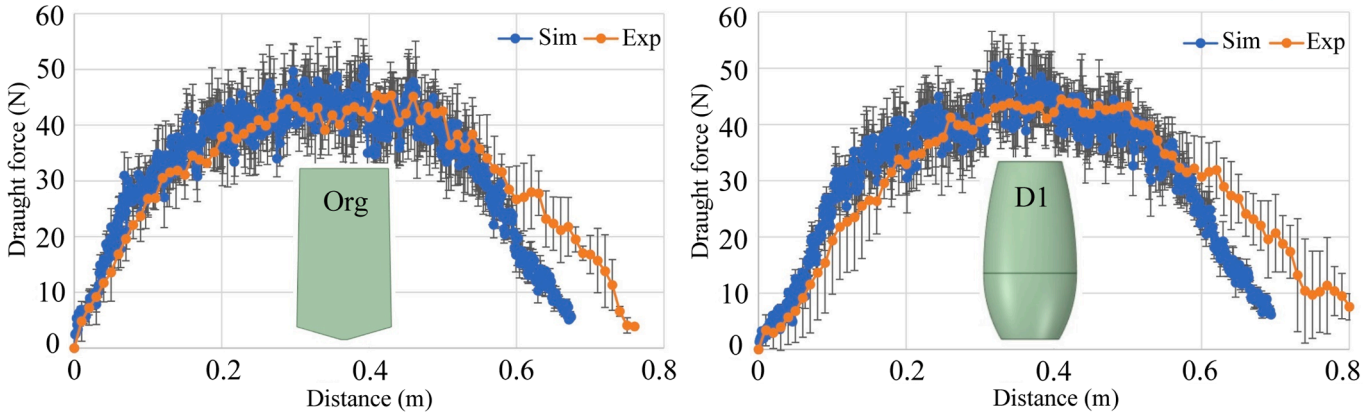

Fig. 11. Draught force of original (Org) and D1 (delta) shape elements obtained from simulation (Sim) and experiment (Exp) in a sand bin.

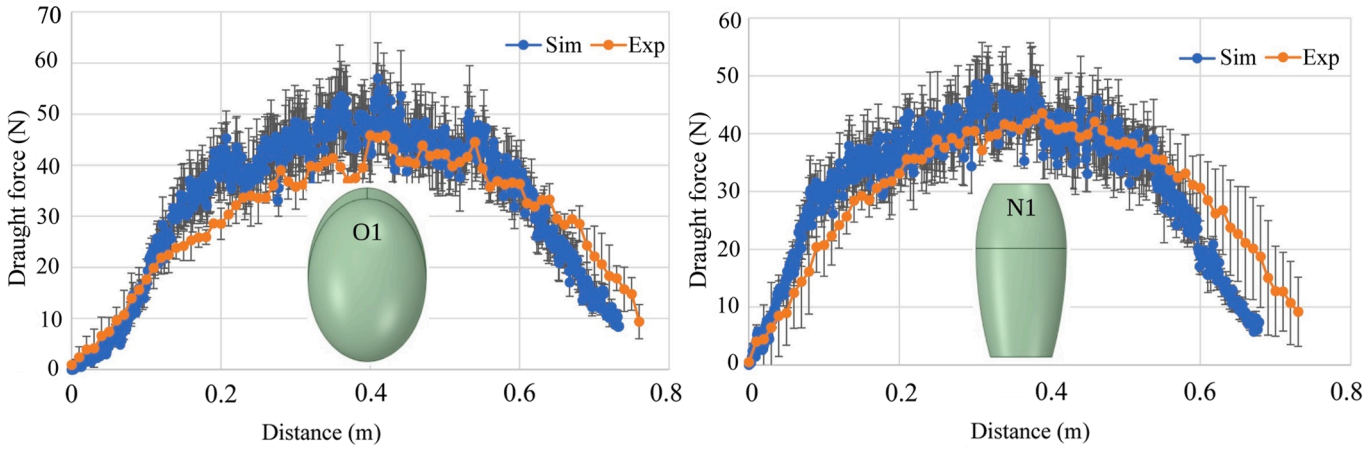

Fig. 12. Draught force of O1 (oval) and N1 (nabla) shape elements obtained from simulation (Sim) and experiment (Exp) in a sand bin.

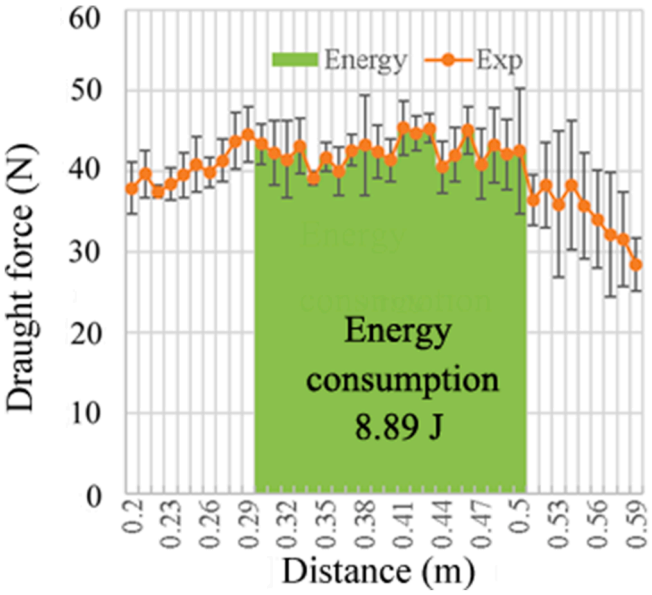

Fig. 13. Energy consumption of original (Org) sample experiment (Exp) measurement in the range of 0.3–0.5 m sand processing distance.

significance level. The energy differences between the simulated and experiment values showed that the simulation for D2 and D3 samples had slightly lower results compared to the experiment (1.4 and 0.2 %). The rest of the simulation results showed a higher energy demand compared to the experiment. The largest differences are found in samples O1, O2 and N5 (8.5, 8 and 6.7 %). This is due to the large number of peaks in the calculation range.

The downward-pointed triangles next to the values (Table 3) indicate that the values in the simulation and experiment measurement are lower compared to the original shape element. Most samples require a slightly lower draught force than the original element shape. The higher draught force in the sand processing was 4.1 and 3.9 % for samples N3 and D3 compared to the original sample, respectively. The laboratory experiments test shows that samples N2, N5, and N1 require a lower draught force of 7.1, 5.7, and 5.2 %, respectively, compared to the original (Org) sample.

Energy consumption follows the trends previously described, with the N2 sample reducing energy consumption by 7.4 %. Except for the sample O4, whose draught force result is closer to the original element, the energy expression increases by 8.5 % in the experimental measurement. This increase in energy is associated with a large number of draught force peaks in the 0.3–0.5 m evaluation interval.

Table 3
Average draught force and energy values of simulation and experiment test in a sand bin in the range of 0.3–0.5 m sand processing distance and sample geometry projection to the direction of motion (the triangle indicates that values are lower or higher compared to the original shape element in each column) (the draught force p-values are lower than the significance level (0.05), except for the O1 and O3 samples).

Sample	Draught force (N)				Energy (J)				Geometry projection area (mm^2)
	Simulation	Change from original (%)	Experiment	Change from original (%)	Simulation	Change from original (%)	Experiment	Change from original (%)	
Original (Org)	44.8 ± 3.17	–	42.4 ± 1.16	–	9.00	–	8.89	–	1511
D1	▼44.5 ± 3.34	−0.7	▼42.0 ± 1.47	−1	▼8.95	−0.6	▼8.78	−1.2	1459
D2	▼42.6 ± 2.66	−5.2	▼42.2 ± 1.22	−0.5	▼8.45	−6.5	▼8.57	−3.7	1393
D3	46.9 ± 3.25	+4.5	44.1 ± 0.78	+3.9	9.24	+2.6	9.26	+4.1	▲1595
O1	46.6 ± 3.62	+3.9	▼41.0 ± 1.25	−3.4	9.37	+3.9	▼8.57	−3.8	1179
O2	47.4 ± 3.17	+5.5	▼41.8 ± 2.23	−1.4	9.53	+5.5	▼8.77	−1.33	1179
O3	44.9 ± 3.81	−0.2	▼42.0 ± 1.09	−1	9.01	+0.1	▼8.75	−1.5	934
O4	▼44.7 ± 3.33	−0.2	▼41.2 ± 0.95	−2.9	9.0	+0.1	9.71	+8.5	▲1526
N1	▼42.1 ± 3.29	−6.4	▼40.3 ± 1.24	−5.2	▼8.86	−1.6	▼8.45	−5.2	1459
N2	▼41.8 ± 3.42	−7.2	▼39.6 ± 0.95	−7.1	▼8.80	−2.3	▼8.27	−7.4	1393
N3	45.2 ± 3.94	+0.9	44.2 ± 1.07	+4.1	9.49	+5.1	9.26	+4.0	▲1595
N4	▼44.6 ± 3.46	−0.5	▼42.1 ± 1.38	−0.7	8.96	−0.5	▼8.81	−0.8	1459
N5	44.9 ± 3.31	+0.2	▼40.1 ± 1.24	−5.7	9.01	+0.1	▼8.41	−5.7	1402
N6	45 ± 3.33	+0.4	42.7 ± 1.58	+0.7	9.05	+0.5	8.95	+0.7	▲1552

3.2. Effect of area projection on draught force

The draught force and energy are influenced by the geometry of the shape and projected area directed to the front surface of the samples. Table 3 shows that samples D3, N3 and N6 have a larger projected area than the original (Org) shape sample. Experiments with wider sweeps (Gürsoy et al., 2017; Ucgul et al., 2014) show that the draught force effect increases due to higher soil resistance, which is consistent with data received in this study. An exception is sample O4, which has a larger projected area but slightly lower draught force values in both experiment and simulation. Sand is a cohesive material that flows easily around the sample (tool), especially if the tool has symmetry in both the vertical and horizontal axes. This characteristic is an advantage of the sample O4, as the sand particles can flow more easily around its surface. Unlike sandy clay or clay, the bottom layer of sand is not compacted. Surprisingly, the projected area of sample O3 is reduced by 32 % compared to the original (Org) shape element, which does not significantly affect the draught force in sand processing. This effect requires more precise analysis to look for a better understanding of soil resistance and tool geometry area dependency. According to the obtain data, can be predicted that draught force and tool contact area has a non-linear dependency, related to the sphere shape of the tool. This prediction requires more analysis in the future experiments.

Likewise, the draught force and energy consumptions recalculated per area unit (Table 4) shows the ratio of force required to process the sand. Due to low values, the force and energy are expressed per m^2. Force per area (N m^{-2}) gives the pressure. The sample O3 has the lowest geometry projection area but draught force is not reduced so much, therefore, ratio of the draught force per projected area and energy are the highest of the tested samples: 41 % higher draught force per area ratio than original shape sample during the simulation, 37.6 % for the experiment measurement in a sand, 38.8 % and 34.4 % higher energy values per area unit at simulation and experiment, respectively. On the other hand, the sample O4 has lower draught force per projected area values for simulation (3 %) and experiment (5.5 %) compared to original sample, while recalculated energy per area values showed that D3 has 2.3 % better results for simulation and 24 % for experiment measurement. According to Archard law (Archard, 1953; Katinas et al., 2021), which is used for the wear simulation, force directly influences material loss changes. Data in Table 4 help to predict wear loss changes for future research and wider analysis of bulbous bow shape elements where the design elements aim would be to disturb the hard soil layers.

3.3. Effect of printing surface roughness

Analysing data between experimental measurement and simulation helps to improve the quality of simulation and obtain more accurate results. As mentioned previously, simulation results have more value than experiment. 3D printed samples have a layered structure outside the body. These layers are caused by the height of print layer. At this time, the height of printing layer of the samples was set as 0.2 mm. The size of the sand particles used for experimental test ranged from 0.1 to 0.3 mm. Smaller particles can be pressed into the corners of the geometry during the experimental test in a sand bin (Fig. 15). In this case, smaller sand particles create a thin shield of particles around the sample (geometry). While small particles “cover” sample (red area in this figure), particle-particle interaction appears. In the absence of small particles around the sample, particle-geometry interaction occurs (yellow area in this figure). This type of interaction dominates in the simulation study for 5 mm particle size. Due to the particle-geometry interaction, the results of the draught force in the simulation are slightly higher compared to the experiment. Such a large size is too large to obtain accurate data but reducing it will prolong computational time and data memory size. By reducing the roughness of printed surface, an accurate result could be obtained. According to (Grabowski et al., 2021) analysis, rough walls and dense sand affect contact forces. The results showed that as the roughness of the walls increases, the non-uniformity of contact forces increases. Horabik and Molenda (Horabik & Molenda, 2016) reviewed the influence of material interaction parameters, where the importance of surface roughness for the simulation results were mentioned.

The printed samples' surface roughness was made to ensure the prediction of particle motion and validate the contact regions. Fig. 16 emphasises surface roughness of the scanned Org and N1 samples. The calculated Rz values are 0.12 and 0.19 mm, respectively. The measured values show that surface irregularities appear in some places where sand particles can be pressed, and particle-to-particle contact regions appear, influencing tool motion properties and values during the sand bin test. The Ra values were not evaluated in this study because needle-based methods often take

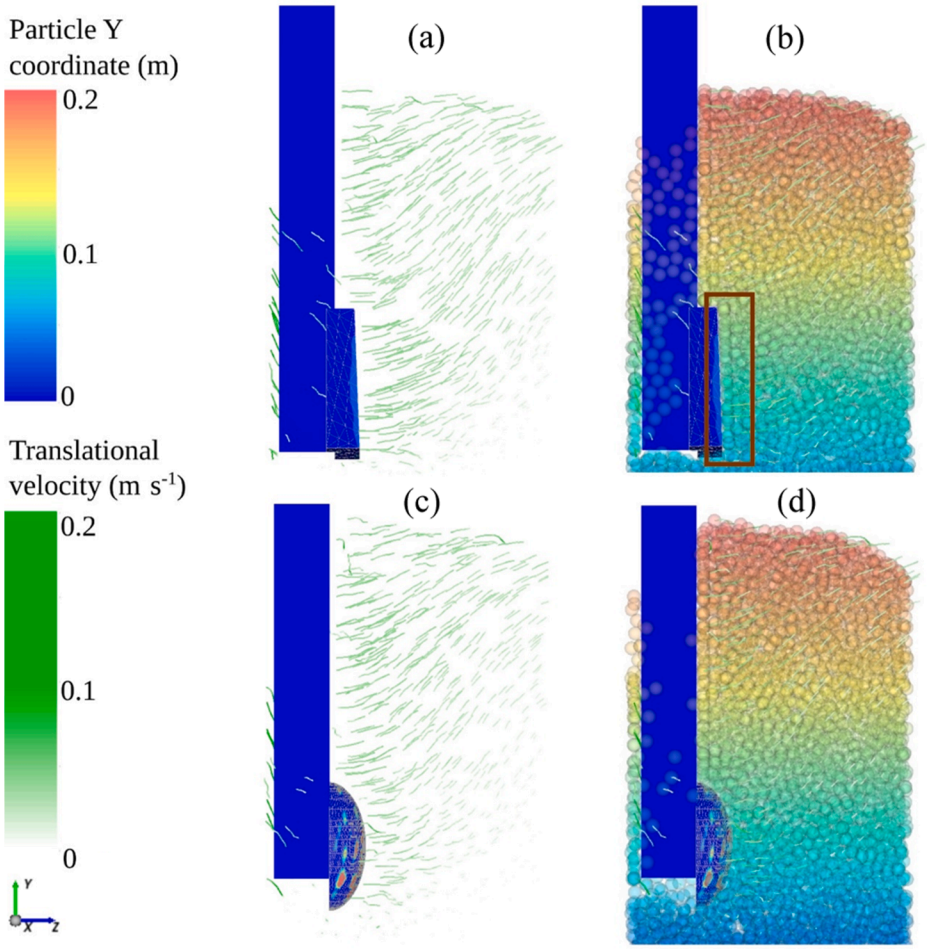

Fig. 14. Particle trajectory during the sand processing of Org (a, b) and O3 (c, d) samples.

Table 4
Draught force and energy values calculated per geometry projection area of each sample.

Sample	Draught force per projected area (N m^{-2})				Energy (J m^{-2})			
	Simulation	Change from original (%)	Experiment	Change from original (%)	Simulation	Change from original (%)	Experiment	Change from original (%)
Original (Org)	28326 ± 148	–	28051 ± 117	–	2886 ± 258	–	3058 ± 380	–
D1	29138 ± 161	+2.8	28752 ± 122	+2.4	2917 ± 268	+1.1	3096 ± 393	+1.2
D2	28799 ± 156	+1.6	30301 ± 125	+7.4	2963 ± 212	+2.6	3139 ± 302	+2.6
D3	27578 ± 175	+2.7	27257 ± 120	−2.9	2822 ± 259	−2.3	2466 ± 327	−24.0
O1	39518 ± 217	+28.3	34709 ± 165	+19.2	4020 ± 437	+28.2	3718 ± 475	+17.8
O2	38522 ± 190	+26.5	35468 ± 167	+20.9	4043 ± 279	+28.6	3858 ± 383	+20.7
O3	48023 ± 288	+41.0	44962 ± 198	+37.6	4713 ± 507	+38.8	4661 ± 515	+34.4
O4	27511 ± 174	−3.0	26592 ± 121	−5.5	2848 ± 358	−1.3	2795 ± 358	−9.4
N1	30218 ± 159	+6.3	27637 ± 126	−1.5	3068 ± 238	+5.9	2993 ± 377	−2.2
N2	30019 ± 173	+5.6	28412 ± 130	+1.3	3088 ± 251	+6.5	3057 ± 387	0.0
N3	28349 ± 174	+0.1	27705 ± 123	−1.2	2902 ± 269	+0.5	2989 ± 379	−2.3
N4	30538 ± 167	+7.2	28807 ± 128	+2.6	3073 ± 239	+6.1	3135 ± 395	+2.4
N5	32011 ± 166	+11.5	28632 ± 134	+2.0	3253 ± 182	+11.3	3106 ± 390	+1.5
N6	29002 ± 152	+2.3	27504 ± 121	−2.0	2920 ± 152	+1.2	3035 ± 373	−0.7

limited 2D profile samples and may not fully reflect the three-dimensional surface variations of the samples being tested. The obstacle is a curved bulbous bow shape. This causes problems in accurately analysing surface irregularities. It is recommended for future studies to improve surface analysis using Ra and Rz measurement values, combining profilometry with 3D optical technologies to provide a more detailed characterisation of surface texture.

From a wear perspective, surfaces with additional inserts, arranged at specific distances and in specified quantities have been shown to reduce wear loss (Grasser et al., 2024). Observations from the three-body abrasion test showed that the thickness of the

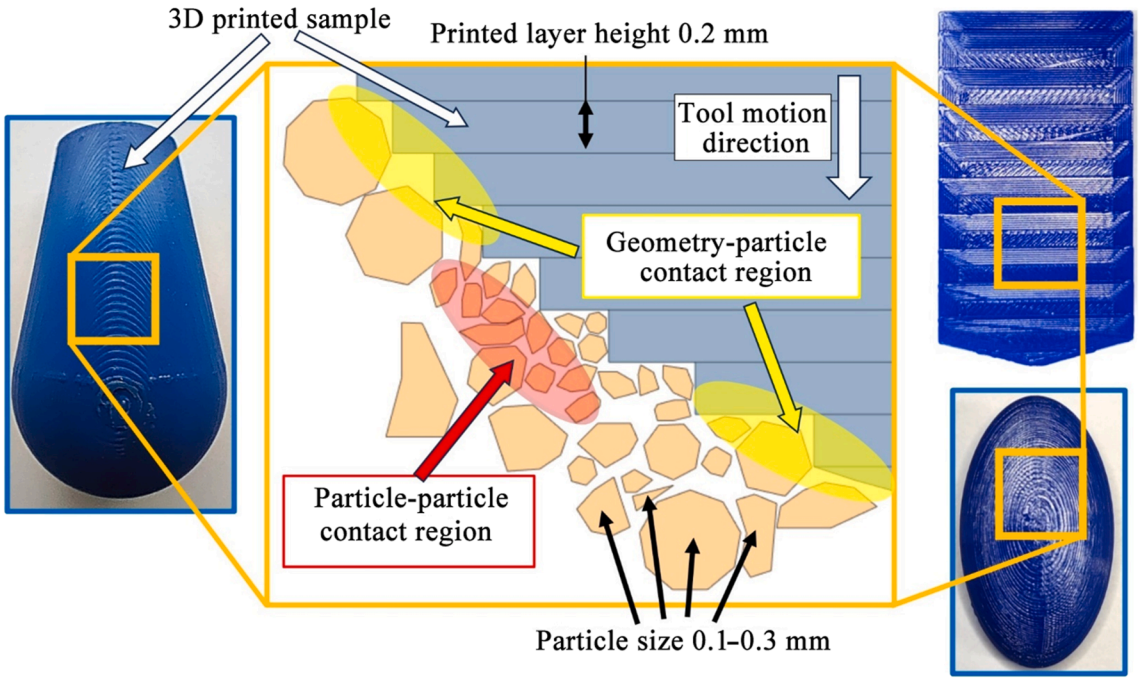

Fig. 15. 3D printed samples (D3, O3 and Org) and particles contact regions.

resulting particle layer affected the particle motion, shifting it from less sliding to more rolling, thereby mitigating surface removal through the micro-ploughing effect. However, the difference in friction forces between surfaces with inserts and smooth surfaces (without inserts) was not measured. Although the operating conditions of the 3D-printed bulbous bow element are different from the aforementioned abrasive conditions, these findings can be applied to enhance wear reduction strategies.

3.4. DEM scaling and sensitivity issue

This scaling away slightly from the actual particle size distribution is typically observed in soil. Increasing the size of DEM particles (in this study was used 5 mm size) can affect the accuracy of modelling micromechanical interactions, such as contact forces and local stress distribution, due to the reduced number of particles and the changed surface-particle interaction. These changes can alter bulk properties such as flowability, density, or shear

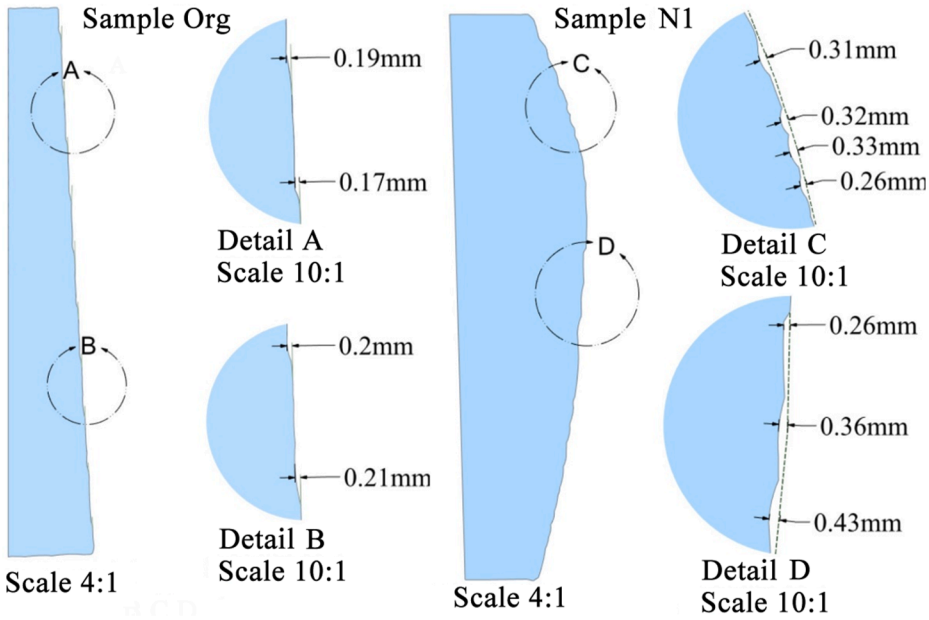

Fig. 16. Surface roughness of 3D printed and scanned Org and N1 samples.

strength. The total generated amount of particles was 0.8 million. Reducing the size of particles (2 and 5 mm) can lead to more accurate analysis, where the particles can be generated by two layers: bottom layer (height 15 cm) with 5 mm size and top layer (where the main contact is between the tool and particles) with 2 mm size of particles (amount of particles increased to 7.3 million). An increasing number of particles drastically increases computational time. For this study, we selected an optimal size of the particles to obtain optimal results based on optimal computational time consumption. For a more accurate analysis, the number of mesh elements of the geometry can be increased, but this option drastically increases the memory usage of the graphics card and, as a result, reaches the limit of the graphics power. In this case, we selected particles of a larger size in the simulation to ensure optimal calculation time and memory consumption. Furthermore, the higher precision results can be reached with lower particle size, higher number of mesh elements and sensitivity analysis based on material interaction properties, which would explain the influence of particle size on the static and dynamic friction of particle-material interaction.

3.5. Future perspectives of designed elements

In addition, the force and energy data generated are suitable for predicting soil processing in the field using a single ripper tool unit (sample and holder). First of all, more tools are processing the soil at the same time (5, 7, 11, 13, etc.), draught force and energy consumption increase depending on the number of tools used. A reduction of a few percent per ripper has an impact on the energy consumption of the entire machine, economic savings, and climate change.

The force results showed that the designed elements do not significantly increase the draught force; in some cases, the force used in sand processing is reduced. The development of such shape elements is primarily aimed at improving wear resistance during soil processing in agriculture. The shape of the working tool can be very complex. However, the essential factor is to retain the energy cost as low as possible and to ensure the agronomic requirements for the processed soil. It should be noted that the oval samples O3 and O4 are versatile. After long work in the soil, the lower part will be worn out more than the upper part. This element can be turned upside down, and the working time will be prolonged.

Further analysis for newly designed elements should focus on wear phenomena when assessing longevity and abrasive wear resistance. Although soil disturbance and particle flow (soil flow) around elements are essential aspects that can be analysed using DEM. Particle flow around the surface can answer abrasive wear resistance of designed elements. The laboratory test in abrasive mass of bulbous bow shape samples will allow to predict the shape changes and see worn elements energy consumption changes. Very interesting information would be gained from the field test where these elements can be tested in loamy or sandy soils. As a final comparison step will help to analyse economic feasibility of designed tools and energy saved during the soil processing at real conditions.

4. Conclusions

This study combined the interdisciplinary approaches from marine engineering and soil processing to investigate the effect of bulbous bow-inspired geometries (delta, oval, and nabla shapes) on soil interaction. The elements were analysed using the Discrete Element Method (DEM) and validated through experimental tests in a sand bin with draught force assessment. The concept of water flow dynamics around bulbous bow elements, which is used in the design of seagoing vessels, has shown potential for reducing energy consumption in soil processing work. Based on the results of the study, the following conclusions are drawn:

- The designed/created elements showed a consistent correlation between the simulation of draught force in sand bin and experimental testing. The simulated draught force values were slightly higher than the experimental data but did not exceed the permissible error limits. The simulation settings and parameters, especially those obtained from repose angle measurements, proved to be effective and can be reliably used in future sand processing simulations.
- In the 0.3–0.5 m processing distance, most of the tested elements showed a reduction in required draught force compared to the original (Org) tool. The nabla-shaped sample N2 showed the greatest improvement, with a 7.1 % reduction in draught force (both simulation and experiment), while sample N3 showed a 4.1 % increase. This shows the importance of geometric refinement even within the same family of shapes.
- The bulbous (spherical) shape tool changed the flow of sand particles compared to the original tool (Org) with a flat surface. The spherical shape of elements encouraged the sand particles to be directed around the tool rather than accumulating directly in front of it (the bulldozer principle), thereby reducing resistance and energy requirements.
- A comparison of the projected tool geometry in the direction of movement showed that, in general, a larger contact area corresponded to higher draught forces. However, the oval-shaped test piece O3, despite having a projected area 32 % smaller than the original tool, did not show a corresponding reduction in draught force, indicating that other factors such as flow dynamics and surface contour also play an important role.

Based on the results of this study, future research should focus on the analysis of abrasive wear and the durability of designed tool shapes under real working conditions. Research into how constant contact with abrasive particles affects tool geometry and efficiency will be very important for practical application. Furthermore, integrating more advanced modelling techniques, such as coupled CFD-DEM models, would provide more detailed information about particle flow dynamics around complex surfaces. It is also recommended to further optimize the design of the shape, considering the choice of materials, energy consumption, and performance scale, to increase the efficiency of the tool in different types of soil and under various working conditions.

CRediT authorship contribution statement

Egidijus Katinas: Writing – review & editing, Writing – original draft, Visualization, Validation, Supervision, Software, Resources, Project administration, Methodology, Investigation, Funding acquisition, Formal analysis, Data curation, Conceptualization. **Regita Bendikienė:** Writing – review & editing, Writing – original draft, Supervision, Resources, Project administration, Methodology, Funding acquisition, Formal analysis, Data curation, Conceptualization. **Antanas Čiuplys:** Project administration, Funding acquisition. **Rostislav Chotěborský:** Validation, Software, Resources. **Monika Hromasová:** Software, Resources. **Barbora Kuřetová:** Investigation.

Funding

This project has received funding from the Research Council of Lithuania (LMTLT), agreement No S-PD-24-31.

Declaration of competing interest

The authors declare that they have no known competing financial interests or personal relationships that could have appeared to influence the work reported in this paper.

References

Adajar, J. B., Alfaro, M., Chen, Y., & Zeng, Z. (2021). Calibration of discrete element parameters of crop residues and their interfaces with soil. *Computers and Electronics in Agriculture, 188*, Article 106349. https://doi.org/10.1016/J.COMPAG.2021.106349

Aikins, K. A., Ucgul, M., Barr, J. B., Awuah, E., Antille, D. L., Jensen, T. A., & Desbiolles, J. M. A. (2023). Review of discrete element method simulations of soil tillage and furrow opening. *Agriculture, 13*(3), 541. https://doi.org/10.3390/AGRICULTURE13030541, 2023, Vol. 13, Page 541.

Ansys. (2024). *Rocky technical manual*.

Archard, J. F. (1953). Contact and rubbing of flat surfaces. *Journal of Applied Physics, 24*(8), 981–988. https://doi.org/10.1063/1.1721448

Bao, M., Lin, J., Zhang, F., & Yang, J. (2023). Discrete element method study of parameter optimization and particle mixing behaviour in a soil mixer. *Particuology, 81*, 1–14. https://doi.org/10.1016/j.partic.2022.12.011

Bao, M., Wu, W., Tian, G., & Qiu, B. (2025). Research on discrete element parameter calibration of ore particles based on tavares breakage model in a SAG mill. *Particuology, 96*, 44–56. https://doi.org/10.1016/J.PARTIC.2024.10.017

Barr, J. B., Ucgul, M., Desbiolles, J. M. A., & Fielke, J. M. (2018). Simulating the effect of rake angle on narrow opener performance with the discrete element method. *Biosystems Engineering, 171*, 1–15. https://doi.org/10.1016/j.biosystemseng.2018.04.013

Bayhan, Y. (2006). Reduction of wear via hardfacing of chisel ploughshare. *Tribology International, 39*(6), 570–574. https://doi.org/10.1016/J.TRIBOINT.2005.06.005

Černilová, B., Kuře, J., Chotěborský, R., & Linda, M. (2024). Particle movement in DEM models and artificial neural network for validation by using contrast points. *Technologies, 12*(12), 257. https://doi.org/10.3390/TECHNOLOGIES12120257, 2024, Vol. 12, Page 257.

Černilová, B., Kuře, J., Linda, M., & Chotěborský, R. (2022). Tracing of the rapeseed movement by using the contrast point tracking method for DEM model verification. *Agronomy Research, 20*(3), 519–530. https://doi.org/10.15159/AR.22.052

Curran-everett, D. (2008). Explorations in statistics : Standard deviations and standard errors. *Advances in Physiology Education, 32*(3), 203–208. https://doi.org/10.1152/advan.90123.2008

Ec.europa.eu. (2024). Agri-environmental indicator - Cropping patterns - Statistics explained. https://ec.europa.eu/eurostat/statistics-explained/index.php?title=Agri-environmental_indicator_-_cropping_patterns&oldid=627430#Data_sources. (Accessed 6 June 2024).

Ge, L., Xu, R., & Nan, W. (2023). Wear of blade spreader during powder spreading in additive manufacturing. *Tribology International, 188*, Article 108818. https://doi.org/10.1016/J.TRIBOINT.2023.108818

Gong, H., Chen, Y., Wu, S., Tang, Z., Liu, C., Wang, Z., … Qi, L. (2022). Simulation of canola seedling emergence dynamics under different soil compaction levels using the discrete element method (DEM). *Soil and Tillage Research, 223*, Article 105461. https://doi.org/10.1016/J.STILL.2022.105461

Grabowski, A., Nitka, M., & Tejchman, J. (2021). 3D DEM simulations of monotonic interface behaviour between cohesionless sand and rigid wall of different roughness. *Acta Geotechnica, 16*(4), 1001–1026. https://doi.org/10.1007/s11440-020-01085-6

Grasser, D., Corujeira Gallo, S., Pereira, M. P., & Barnett, M. (2024). Wear simulation and validation of composites (insert-reinforced matrix) in the dry sand rubber wheel test. *Minerals Engineering, 207*, Article 108583. https://doi.org/10.1016/J.MINENG.2024.108583

Guan, C., Fu, J., Xu, L., Jiang, X., Wang, S., & Cui, Z. (2022). Study on the reduction of soil adhesion and tillage force of bionic cutter teeth in secondary soil crushing. *Biosystems Engineering, 213*, 133–147. https://doi.org/10.1016/J.BIOSYSTEMSENG.2021.11.018

Gürsoy, S., Chen, Y., & Li, B. (2017). Measurement and modelling of soil displacement from sweeps with different cutting widths. *Biosystems Engineering, 161*, 1–13. https://doi.org/10.1016/J.BIOSYSTEMSENG.2017.06.005

Guyomard, H., Bureau, J., Chatellier, V., Detang-Dessendre, C., Dupraz, P., Jacquet, F., … Tysebaert, M. (2020). *Research for AGRI committee - The green deal and the CAP: Policy implications to adapt farming practices and to preserve the EU's natural resources*. Brussels.

Horabik, J., & Molenda, M. (2016). Parameters and contact models for DEM simulations of agricultural granular materials: A review. *Biosystems Engineering, 147*, 206–225. https://doi.org/10.1016/J.BIOSYSTEMSENG.2016.02.017

Hoyle, J. W. (1985). Optimization of bow-bulb for resistance and seakeeping characteristics. Retrieved from https://apps.dtic.mil/sti/tr/pdf/ADA158831.pdf.

Jankauskas, V., Katinas, E., Skirkus, R., & Aleknevičiene, V. (2014). Friction and wear the method of hardening soil rippers by surfacing. *Journal of Friction and Wear, 35*(4), 421–430.

Jiang, X., Tong, J., Ma, Y., & Sun, J. (2020). Development and verification of a mathematical model for the specific resistance of a curved subsoiler. *Biosystems Engineering, 190*, 107–119. https://doi.org/10.1016/J.BIOSYSTEMSENG.2019.12.004

Just, S., Toschkoff, G., Funke, A., Djuric, D., Scharrer, G., Khinast, J., … Kleinebudde, P. (2013). Experimental analysis of tablet properties for discrete element modeling of an active coating process. *AAPS PharmSciTech, 14*(1), 402–411. https://doi.org/10.1208/s12249-013-9925-5

Kalácska, Á., De Baets, P., Fauconnier, D., Schramm, F., Frerichs, L., & Sukumaran, J. (2020). Abrasive wear behaviour of 27MnB5 steel used in agricultural tines. *Wear, 442–443*, Article 203107. https://doi.org/10.1016/j.wear.2019.203107

Katinas, E., Bendikienė, R., Jankauskas, V., & Čiuplys, A. (2024). The bulbous bow shape adaptability for the soil ripper tool. *Agricultural Engineering 2024*, 880–887.

Katinas, E., Chotěborský, R., Linda, M., & Jankauskas, V. (2019). Wear modelling of soil ripper tine in sand and sandy clay by discrete element method. *Biosystems Engineering, 188*, 305–319. https://doi.org/10.1016/j.biosystemseng.2019.10.022

Katinas, E., Chotěborský, R., Linda, M., & Kuře, J. (2021). Sensitivity analysis of the influence of particle dynamic friction, rolling resistance and volume/shear work ratio on wear loss and friction force using DEM model of dry sand rubber wheel test. *Tribology International, 156*, Article 106853. https://doi.org/10.1016/j.triboint.2021.106853

Kostencki, P., Stawicki, T., & Bialobrzeska, B. (2016). Durability and wear geometry of subsoiler shanks provided with sintered carbide plates. *Tribology International, 104*, 19–35. https://doi.org/10.1016/j.triboint.2016.08.020

Kracht, A. (1978). Design of bulbous bows. *SNAME Transactions, 86*, 197–217.

Kuře, J., Linda, M., Chotěborský, R., Černilová, B., & Hromasová, M. (2021). DEM modelling of tillage tools in sand and verification of draft forces in the soil box. *Agronomy Research, 19*(4), 1813–1822. https://doi.org/10.15159/AR.21.147

Li, B., Chen, Y., & Chen, J. (2016). Modeling of soil–claw interaction using the discrete element method (DEM). *Soil and Tillage Research, 158*, 177–185. https://doi.org/10.1016/J.STILL.2015.12.010

Liu, K., Sozzi, M., Gasparini, F., Marinello, F., & Sartori, L. (2023). Combining simulations and field experiments: Effects of subsoiling angle and tillage depth on soil structure and energy requirements. *Computers and Electronics in Agriculture, 214*, Article 108323. https://doi.org/10.1016/J.COMPAG.2023.108323

Liu, X., Zhao, W., & Wan, D. (2021). Hull form optimization based on calm-water wave drag with or without generating bulbous bow. *Applied Ocean Research, 116*, Article 102861. https://doi.org/10.1016/J.APOR.2021.102861

Ma, S., Xu, L., Xu, S., Tan, H., Song, J., & Shen, C. (2023). Wear study on flexible brush-type soil removal component for removing soil used to protect grapevines against cold. *Biosystems Engineering, 228*, 88–104. https://doi.org/10.1016/J.BIOSYSTEMSENG.2023.03.001

Makange, N. R., Ji, C., & Torotwa, I. (2020). Prediction of cutting forces and soil behavior with discrete element simulation. *Computers and Electronics in Agriculture, 179*, Article 105848. https://doi.org/10.1016/j.compag.2020.105848

Mehrang Marani, S., Shahgholi, G., & Moinfar, A. (2019). Effect of nano coating materials on reduction of soil adhesion and external friction. *Soil and Tillage Research, 193*(November 2018), 42–49. https://doi.org/10.1016/j.still.2019.05.026

Natsis, A., Petropoulos, G., & Pandazaras, C. (2008). Influence of local soil conditions on mouldboard ploughshare abrasive wear. *Tribology International, 41*(3), 151–157. https://doi.org/10.1016/J.TRIBOINT.2007.06.002

Nouh, S. A., KuShaari, K. Z., Keong, L. K., & Samsuri, S. (2024). Material characterization and inter/intra-particle validation for DEM simulation of urea coating process. *Particuology, 88*, 32–48. https://doi.org/10.1016/j.partic.2023.09.010

Roessler, T., & Katterfeld, A. (2016). Scalability of angle of repose tests for the calibration of DEM parameters. In *ICBMH 2016 - 12th International Conference on Bulk Materials Storage, Handling and Transportation, Proceedings, (November)* (pp. 201–211).

Sang, H., He, C., Bi, Y., Liu, M., & Wang, X. (2022). Evaluation of the performance of very narrow tines with different geometrical structures for tilling natural grassland. *Biosystems Engineering, 224*, 34–48. https://doi.org/10.1016/J.BIOSYSTEMSENG.2022.09.011

Šarauskis, E., Romaneckas, K., Kumhála, F., & Kriaučiūnienė, Z. (2018). Energy use and carbon emission of conventional and organic sugar beet farming. *Journal of Cleaner Production, 201*, 428–438. https://doi.org/10.1016/J.JCLEPRO.2018.08.077

Schramm, F., Kalácska, Á., Pfeiffer, V., Sukumaran, J., De Baets, P., & Frerichs, L. (2020). Modelling of abrasive material loss at soil tillage via scratch test with the discrete element method. *Journal of Terramechanics, 91*, 275–283. https://doi.org/10.1016/j.jterra.2020.08.002

Skirkus, R., Jankauskas, V., & Gaidys, R. (2016). Estimating stresses and movement work of a soil-cultivator tip using the finite-element method. *Journal of Friction and Wear, 37*(5), 489–493. https://doi.org/10.3103/S1068366616050172

Sun, J., Chen, H., Wang, Z., Ou, Z., Yang, Z., liu, Z., & Duan, J. (2020). Study on plowing performance of EDEM low-resistance animal bionic device based on red soil. *Soil and Tillage Research, 196*, Article 104336. https://doi.org/10.1016/J.STILL.2019.104336

Tran, T. G., Van Huynh, C., & Kim, H. C. (2021). Optimal design method of bulbous bow for fishing vessels. *International Journal of Naval Architecture and Ocean Engineering, 13*, 858–876. https://doi.org/10.1016/J.IJNAOE.2021.10.006

Ucgul, M., Fielke, J. M., & Saunders, C. (2014). 3D DEM tillage simulation: Validation of a hysteretic spring (plastic) contact model for a sweep tool operating in a cohesionless soil. *Soil and Tillage Research, 144*, 220–227. https://doi.org/10.1016/J.STILL.2013.10.003

Walton, O. R., & Braun, R. L. (1986). Viscosity, granular-temperature, and stress calculations for shearing assemblies of inelastic, frictional disks. *Journal of Rheology, 30*(5), 949–980. https://doi.org/10.1122/1.549893

Wang, Y., Li, N., Ma, Y., Tong, J., Pfleging, W., & Sun, J. (2020). Field experiments evaluating a biomimetic shark-inspired (BioS) subsoiler for tillage resistance reduction. *Soil and Tillage Research, 196*, Article 104432. https://doi.org/10.1016/J.STILL.2019.104432

Wang, Y., Xue, W., Ma, Y., Tong, J., Liu, X., & Sun, J. (2019). DEM and soil bin study on a biomimetic disc furrow opener. *Computers and Electronics in Agriculture, 156*, 209–216. https://doi.org/10.1016/J.COMPAG.2018.11.023

Wang, X., Zhou, H., Wang, S., Zhou, H., & Ji, J. (2023). Methods for reducing the tillage force of subsoiling tools: A review. *Soil and Tillage Research, 229*, Article 105676. https://doi.org/10.1016/J.STILL.2023.105676

Wensrich, C. M., & Katterfeld, A. (2012). Rolling friction as a technique for modelling particle shape in DEM. *Powder Technology, 217*, 409–417. https://doi.org/10.1016/j.powtec.2011.10.057

Xie, C., Zhao, Y., Song, T., & Zhao, Y. (2022). Investigation of the effect of filling level on the wear and vibration of a SAG mill by DEM. *Particuology, 63*, 24–34. https://doi.org/10.1016/J.PARTIC.2021.04.009

Xu, Z., Qi, H., Gao, P., Wang, S., Liu, X., & Ma, Y. (2024). Biomimetic design of soil-engaging components: A review. *Biomimetics, 9*(6), 358. https://doi.org/10.3390/BIOMIMETICS9060358, 2024, Vol. 9, Page 358.

Xu, G., Zhang, Y., Yang, X., Chen, G., & Jin, B. (2023). Effect of drum structure on particle mixing behavior based on DEM method. *Particuology, 74*, 74–91. https://doi.org/10.1016/j.partic.2022.05.008

Yao, Q., Han, X., Hu, Y., Guo, Z., Fan, P., & Zhang, Y. (2024). Field wear tests of ploughshares in the southern Xinjiang region. *Engineering Failure Analysis, 163*, Article 108522. https://doi.org/10.1016/J.ENGFAILANAL.2024.108522

Zhang, C., Wang, X., Guo, M., Zhao, J., & Li, M. (2024). A compacting device of rice dry direct-seeding planter based on DEM-MFBD coupling simulation significantly improves the seedbed uniformity and seedling emergence rate. *Biosystems Engineering, 246*, 26–40. https://doi.org/10.1016/J.BIOSYSTEMSENG.2024.07.018

Zhang, L., Zhai, Y., Chen, J., Zhang, Z., & Huang, S. (2022). Optimization design and performance study of a subsoiler underlying the tea garden subsoiling mechanism based on bionics and EDEM. *Soil and Tillage Research, 220*, Article 105375. https://doi.org/10.1016/J.STILL.2022.105375

Zhao, J., Yu, J., Sun, K., Wang, Y., Liang, L., Sun, Y., … Yu, Y. (2024). A discrete element method model and experimental verification for wheat root systems. *Biosystems Engineering, 244*, 146–165. https://doi.org/10.1016/J.BIOSYSTEMSENG.2024.06.004